Simulated synthesis and atomic-level structural characterization of $LiNi_2O_4$

Donald Hlungwani*, *Raesibe Sylvia* Ledwaba, and *Phuti* Ngoepe

Materials Modelling Centre, University of Limpopo, Private Bag x1106, Sovenga 0727, South Africa

Abstract. $LiMn_2O_4$ is a promising cathode material for advancing lithium-ion batteries due to its high-rate capabilities and high operating voltages. However, it suffers capacity fading due to the loss of manganese and lattice instabilities linked to Mn^{3+} during cycling. The simulated synthesis technique has been used to generate $LiNi_2O_4$ models rich in microstructural features that evolve during the crystal growth process. The microstructural features can be linked to the electrochemical performance and properties of $LiNi_2O_4$, which will guide the doping of $LiMn_2O_4$ spinel with Ni. Substitution of a small amount of manganese with nickel has been proposed as one of the solutions for reducing capacity loss. The $LiNi_2O_4$ spinel structure was synthesized successfully with the simulated amorphization and recrystallization technique. The RDF functions indicated the average Ni – O bond length of ~1.925 Å which is comparable to the Ni – O average bond length of ~1.923 Å synthesized by Thomas M.G.SR and co-workers.

1. Introduction

The positive electrode material in lithium-ion batteries has been reported as a major limiting factor in terms of their performance [1-3]. Significant research efforts have been delegated to finding suitable positive electrode materials due to the increasing energy demand caused by exponential technological advancement, the need for renewable energy storage, and the emerging hybrid electric vehicles (HEVs) and electric vehicles (EVs). Transition metal-based cathode materials that crystallize into layered or spinel structures have been largely considered for lithium-ion batteries due to their ability to intercalate lithium ions at acceptable voltages. Lithium-cobalt-oxide $LiCoO_2$ which crystallizes into a layered structure (alpha-$NaFeO_2$) has been a positive electrode material of choice since the inception of lithium-ion batteries. Despite its commercial success, its performance falls short for large-scale applications such as HEVs and EVs. $LiCoO_2$ is not cost-effective, most of its capacity can only be obtained at high operating voltages which leads to structural instabilities. In addition, it is reported to suffer from thermal stability, and to be toxic [4-7].

$LiNiO_2$ has also been investigated as a prospective cathode material for LIBs. $LiNiO_2$ is a better electrode material than $LiCoO_2$ in terms of cost and energy density. However, it exhibits inferior cycling performance linked to the instability and high reactivity of the Ni^{4+} ions [8-10]. Layered cathode materials that are rich in lithium and manganese content have

* Corresponding author: donald.hlungwani@gmail.com

also been investigated for large-scale commercial applications due to their cost effectiveness. $xLi_2MnO_3 \cdot (1\text{-}x)\ LiMO_3$ (M = Mn, Ni, Co, etc.) can deliver high practical capacities between 2.0 and 4.8 V making it attractive for application in HEVs, EVs, and smart-grids. Their commercial application has been delayed by poor rate capabilities and inferior cyclic performance associated with the loss of oxygen during the activation process, and irreversible phase transitions [11-13]. Lithium-manganese-oxide ($LiMn_2O_4$) with a spinel structure has also gained enormous attention because it is economically viable, environmentally benign, exhibits high-rate capabilities, and is relatively thermally stable. The material consists of oxygen atoms which are closely packed forming a cubic structure, manganese atoms occupying the octahedral sites, and lithium atoms situated at the tetrahedral sites. Moreover, the structure has a space group of Fd-3m and allows the extraction and insertion of lithium ions through three-dimensional diffusion channels enabling high-rate capabilities. However, the commercialization of this material has been delayed. $LiMn_2O_4$ spinel suffers structural stability associated with irreversible phase transitions, disproportionation reaction of Mn^{3+}, and the onset Jahn-Teller distortion linked with high spine Mn^{3+}, particularly at elevated temperatures [14-16].

Surface modification and cation doping have been reported as the most effective approaches for enhancing the cyclic performance of various cathode materials. Several reports have suggested that the replacement of a small amount of manganese with cations such as Ni, Co, Al, etc. could stabilize the $LiMn_2O_4$ spinel structure during cycling. Xiong L et al. observed an improvement in the structure of $LiMn_2O_4$ spinel due to a small substitution of Ti ions into the octahedral sites of Mn ions. Moreover, the charge resistance and diffusion coefficient of the material were enhanced [17]. Iwata and co-workers found that the Cr-doped $LiMn_2O_4$ spinel has better cycle performance than the pristine $LiMn_2O_4$ spinel [18]. Moreover, Thackeray and co-workers suggested that doping $LiMn_2O_4$ spinel with Co, Ni, Cr, etc. could improve structural stability if the resulting M-O (M = Co, Ni, Cr) bond is stronger than the Mn-O bond [19]. However, there's insufficient knowledge of the effect of cation doping on the microstructure of $LiMn_2O_4$ spinel, particularly with Ni. Hence, we perform large-scale atomistic simulations of $LiNi_2O_4$ spinel to direct the doping of $LiMn_2O_4$ spinel with Ni.

2. Methodology

This work has been performed computationally using the classical mechanics method, molecular dynamics. The energy of interaction for the atoms in the $LiNi_2O_4$ spinel is described by the Buckingham potential (BP) function. The calculations were performed with the DL_POLY code, which has been widely used to study systems at the microscale [17].

2.1 Generation of the simulation models

A 56-atom $LiNi_2O_4$ conventional unit cell was used to construct a $LiNi_2O_4$ nanosphere containing 3846 Li atoms, 7676 Ni atoms, and 15184 O atoms. The 8.3 nm spherical LiN_2O_4 spinel structure was generated and optimized with the METADISE program [20]. Furthermore, DL_POLY input files of the ground state structure were also generated with the METADISE code [20]. The lattice constant of the $LiNi_2O_4$ conventional unit cell used is 8.123 Å, which is comparable to a lattice parameter of 8.157 Å calculated by Kuwabara A et al [21]. The conventional spinel $LiNi_2O_4$ unit cell consists of Ni atoms in the octahedral sites, Li atoms in the tetrahedral sites, and O atoms situated at the 32e sites.

2.2 Potential model

The lattice energy is described by the Born model of ionic solids for the ionic interactions in the $LiNi_2O_4$ structure. The model describes the energy contribution due to electrostatic interactions and the short-range repulsive energy. The short-repulsive energy contribution represents the van der Waals interactions and ensures that the ionic spheres do not overlap. Moreover, the electrostatic energy of interaction is given by Coulombic interaction. In this work, the non-bonded van der Waals interactions are described by the Buckingham potential function. The parameters of the Buckingham potential function are determined from experimental data. The Li-Li, Li-O, and O-O Buckingham potentials used in this study were determined and tested elsewhere [22-23]. Additionally, we have derived the Buckingham potential for the Ni-O, Ni-Ni, and Ni-Li potentials utilized in this study [24]. Partial atomic charges are employed for the electrostatic interactions.

2.3 Simulate synthesis method.

A simulated synthesis technique is employed to generate a spinel $LiNi_2O_4$ nanosphere comprising essential structural features comparable to those of materials in experiments [25]. The technique involves simulated amorphization, which is followed by simulated recrystallization. The simulated amorphization is carried out under a constant number of particles, confined to a constant volume, where the total energy of the system is kept constant. The simulated recrystallization is performed under a canonical ensemble, which is characterized by a constant number of particles confined to a non-changing volume where the temperature of the system is kept constant. The simulated recrystallization is followed by systematic cooling of the recrystallized structure. All the molecular dynamics calculations in this study were performed with the Nose-Hoover thermostat. The time per step of 1e-16 s and 3e-15 s were chosen for amorphization and recrystallization, respectively. The systems taken into consideration were allowed to equilibrate for 50 000 steps, and the Ewald summation method with a cutoff radius of 10 Å was chosen.

3. Results and Discussion

A 26706-atom $LiNi_2O_4$ spinel nanosphere has been prepared with the amorphization and recrystallization (A&R) technique. A&R is a simulated synthesis method essential for generating models that comprise essential structural features that are likely to be observed in experiments. Figure 1 shows the procedure for generating the $LiNi_2O_4$ amorphous spinel structure. The nanospherical and crystalline $LiNi_2O_4$ illustrated in Figure 1 (b) was cleaved from a 56-atom $LiNi_2O_4$ conventional unit cell shown in Figure 1 (a). The successful simulated amorphization was confirmed through the radial distribution functions (RDFs) of the Ni-O interaction illustrated in Figure 2. The first neighbor distance is observed at a separation distance of ~1.925 Å. The probability of finding a Ni atom with respect to O atoms is significantly greater than zero from the separation distance of 1.5 Å. Moreover, the absence of discrete peaks from the separation distance of 1.5 Å indicates a lack of long-range atomic ordering in the structure. Furthermore, only the first coordination shell can be distinctively observed in the RDF, as such the $LiNi_2O_4$ structure is in an amorphous state. Therefore, the spinel $LiNi_2O_4$ nanostructure amorphized at a temperature of 1900 K.

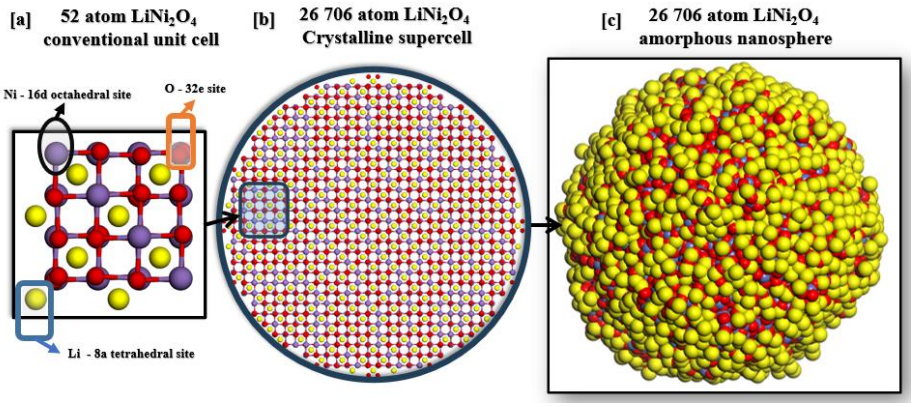

Fig. 1. Illustration of the process of obtaining amorphous $LiNi_2O_4$ spinel. (a) A 56-atom $LiNi_2O_4$ is cleaved to form (b) a 26706-atom $LiNi_2O_4$ nanospherical supercell. The nanospherical crystalline $LiNi_2O_4$ spinel structure is amorphized under the NVE ensemble to yield the amorphous structure in (c). The simulated amorphization of a 26706-atom $LiNi_2O_4$ spinel nanostructure. (a) A conventional unit

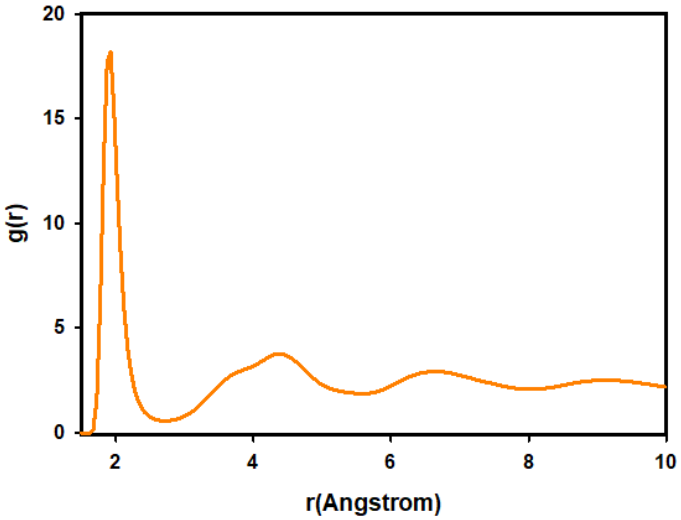

Fig. 2. Radial distribution functions (RDF) of the Ni-O interaction delineate the amorphous state of the $LiNi_2O_4$ nanosphere.

The amorphous structure in Figure 1(c) was further recrystallized under the canonical ensemble at temperatures of 1700 K, 1800 K, and 1900 K. Patterns of Ni and O atoms can be noted from the $LiNi_2O_4$ structures recrystallized at 1800 K and 1900 K in Figure 3. The structure recrystallized at 1700 K shows no patterns of Ni and O atoms, indicating that the structure is in an amorphous state. Figure 4 illustrates the recrystallization of the $LiNi_2O_4$ spinel at temperatures of 1700 K, 1800 K, and 1900 K through RDFs. The structure of $LiNi_2O_4$ spinel is given by the interaction between Ni and O, hence, the RDFs of the Ni-O interaction have been chosen to capture the state of the material. The second and third coordination shells can be noted from the RDF graphs of the $LiNi_2O_4$ spinel structure at 1800 K and 1900 K, respectively. Hence, the structures possess long-range atomic ordering. Figure 4 (b) compares the RDF of the different temperatures (1700 K, 1800 K, and 1900 K) between the separation distances of 3.0 and 5.5 Å. At a separation distance of ~ 4.0 Å, the probability

of finding Ni atoms with O as the reference atoms is low for the structure recrystallized at a temperature of 1900 K. Therefore, the $LiNi_2O_4$ spinel structure recrystallizes well at a temperature of 1900 K. Furthermore, this structure was then cooled to a temperature of 5 K to reduce the vibration of the atoms about their lattice positions. The RDF of the cooled $LiNi_2O_4$ structure is shown in Figure 4 (c). A sharp peak of the first coordination shell is noted at the atomic separation of ~1.925 Å. As such, the average bond length of Ni-O is ~1.925 Å, which is comparable to the Ni-O average bond length determined by Thomas M.G.S.R and co-workers [26]. Furthermore, two distinctive RDF peaks that follow the first RDF peak are also observed. The two peaks illustrate the presence of long-range atomic ordering in the cooled $LiNi_2O_4$ spinel structure. Moreover, the probability of finding atoms between these two peaks is close to zero, evidencing the reduction of atomic vibrations about lattice position during cooling.

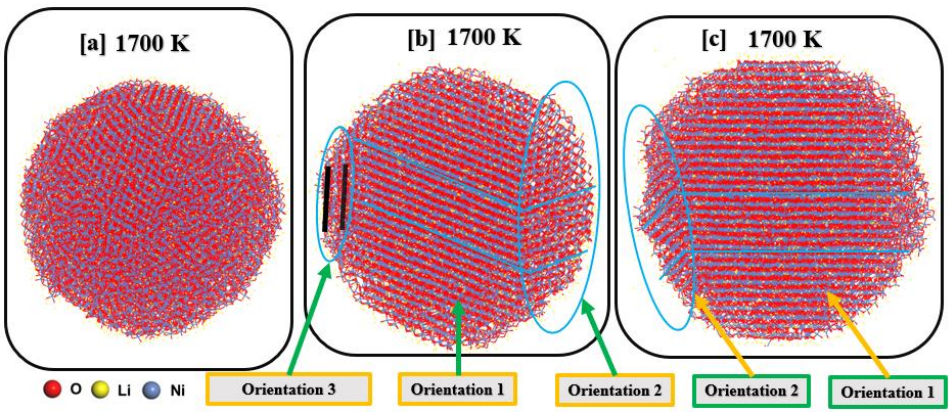

Fig. 3. Atomic snapshots illustrating the recrystallization of the $LiNi_2O_4$ spinel nanosphere at temperatures of (a) 1700 K, (b) 1800 K, and (c) 1900 K.

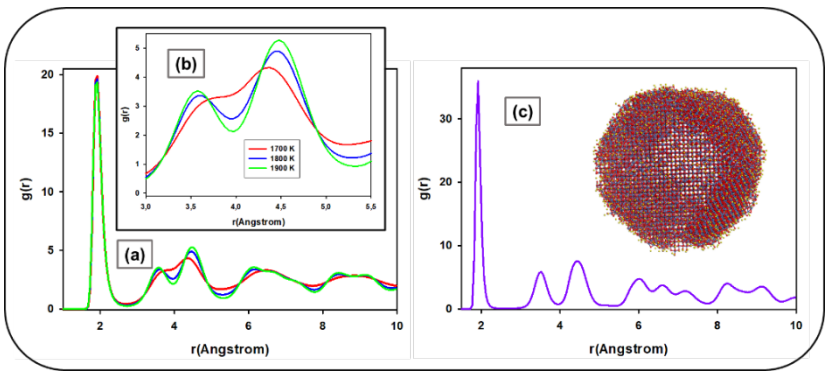

Fig. 4. RDFs of the recrystallization of $LiNi_2O_4$ spinel at (a) 1700 K, 1800 K, and 1900 K for the Ni-O interaction. (b) A magnified portion of the RDFs of $LiNi_2O_4$ at temperatures of 1700 K, 1800 K, and 1900 K. (c) The RDF of the $LiNi_2O_4$ spinel structure recrystallized at a temperature of 1900 K and cooled to a temperature of 5 K.

Figure 5 illustrates the characterization of the $LiNi_2O_4$ spinel recrystallized at 1900 K. Several layers of Ni, O, and Li have been extracted from the nanosphere to demonstrate the spinel phases that formed during the simulated synthesis. Figure 5 (a) illustrates the presence of a spinel phase characterized by a layer of alternating Li and O atoms in between two layers of alternating Li, O, and Ni atoms. The same pattern is observed in the theoretical model of

the spinel illustrated in Figure 5 (b). Furthermore, the spinel phase is also characterized by a layer of Ni and Li atoms, wherein every Li atom is followed by three Ni atoms in between two layers of oxygen atoms. Figure 5 (d) and (e) compare the simulated and theoretical spinel phases defined by the latter layer pattern. In addition, a conventional unit cell view of the spinel phase has also been captured and illustrated in Figure 5 (g). The conventional unit cell possesses lattice defects such as substitution. This conventional unit cell is comparable to a theoretical $LiNi_2O_4$ spinel conventional unit cell containing Li atoms at the 16c octahedral sites shown in Figure 5 (h). The atomic snapshots also reveal the presence of the Ni_3O_4 impurity phase in the structure, as evinced by the presence of Ni atoms in the 8a tetrahedral sites demonstrated in Figure 5 (k). The simulated $LiNi_2O_4$ spinel nanostructure was further characterized through x-ray diffraction (XRD) patterns. The XRD pattern of the $LiNi_2O_4$ spinel generated through the A&R is shown in Figure 6 (i). XRD peaks are observed at ~18°, ~30°, ~37°, ~45°, ~47°, 60°, 65° 2θ degrees on the illustrated pattern of $LiNi_2O_4$ spinel. The XRD peaks can be indexed to a cubic spinel structure. The XRD peak at ~30° 2θ degrees is attributed to the Ni_3O_4 impurity phase. Figure 6(ii) shows the XRD patterns of $LiNi_2O_4$ synthesized experimentally [26]. The XRD pattern compares well to the XRD pattern of the simulated structure. The formation of the M_3O_4 impurity phase at elevated temperatures has been noted in various studies of LiM_2O_4 (M = Co, Ni, Mn, etc.) spinel systems [27-30].

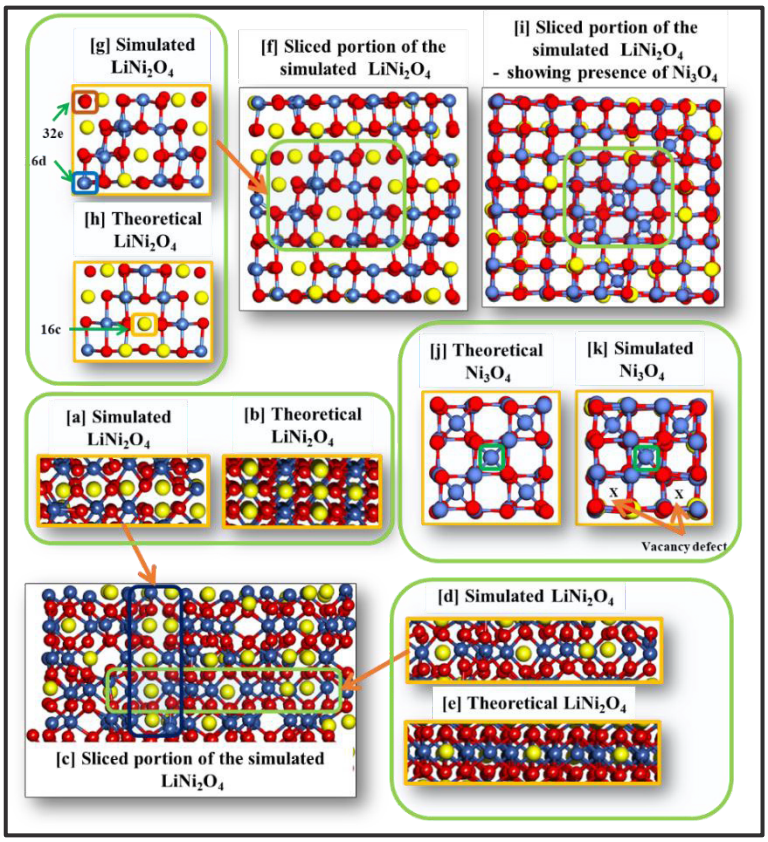

Fig. 5. Structural characterization of the A&R simulated $LiNi_2O_4$ spinel. (c), (f), and (i) Atomic layers in the $LiNi_2O_4$ spinel structure have been sliced to illustrate the spinel phases that formed during recrystallization. The spinel phases that formed during simulated A&R are compared to their respective theoretical models.

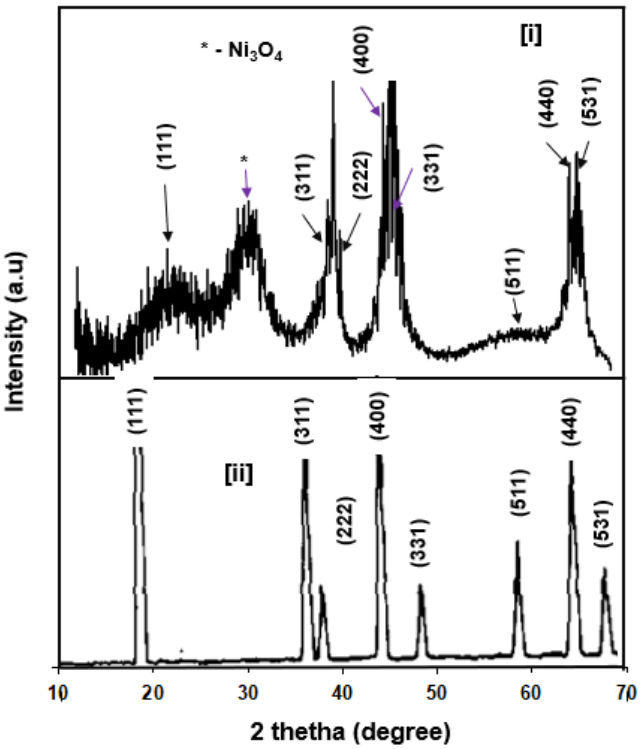

Fig. 6. Comparison of the X-ray diffraction (XRD) patterns of the (i) A&R-simulated (this work) and (ii) experimental $LiNi_2O_4$ spinel [26].

4. Conclusion

The simulated synthesis (A&R) was used to generate $LiNi_2O_4$ spinel nanostructure. The generated structure was further characterized through RDFs, atomic snapshots, and XRD graphs. The $LiNi_2O_4$ spinel structure was found to recrystallize at temperatures of 1800 K and 1900 K, and it was found to be more crystalline at 1900 K. The formation of the $LiNi_2O_4$ spinel phase was confirmed by atomic snapshots and X-ray diffraction patterns. Furthermore, the Ni_3O_4 impurity phase was observed at elevated temperatures, the same behaviour is also observed in lithium-manganese-oxide spinel structures. In addition, the Ni-O bond length was found to be ~1.925 Å which is less than the average bond length of the Mn-O bond length of ~1.937 Å [31]. Therefore, a stronger M-O bond could be realized when M = Ni than when M = Mn. Hence, a substitution of a small amount of Ni in the $LiMn_2O_4$ spinel structure could improve structural stability.

References

1. J. Xu J, S. Dou, H. Liu, L. Dai, Nano Energy **2**, 439-442 (2013)
2. Z. Lu, D.D. MacNeil, J.R. Dahn **4**, A191-A191 (2001)
3. B. Xu, D. Qian, Z. Wang, Y.S Meng, Mater. Sci. Eng. R Rep **73**, 51-65 (2012)
4. G.G. Amatucci, J.M. Tarascon, L.C. Klein, Solid State Ionics **83**, 167-173 (1996)
5. G.T.K Fey, R.F. Shiu, T.P. Kumar, C.L. Chen, *Mater. Sci. Eng. B* **100**, 234-243 (2003)

6. J.C. Zhang, Z.D. Liu, C.H. Zeng, J.W. Luo, Y.D. Deng, X.Y. Cui, Y.N. Chen, Rare Met **41**, 3946-3956 (2022)
7. S.D. Zhang, M.Y. Qi, S.J. Guo, Y.G. Sun, X.X. Tan, P.Z. Ma, J.Y. Li, R.Z. Yuan, A.M. Cao, L.J. Wan, Small Methods **6**, 2200148-2200148 (2022)
8. G.X. Huang, R.H. Wang, X.Y. Lv, J. Su, Y.F. Long, Z.Z. Qin, Y.X. Wen, *J. Electrochem. Soc.* **169**, 040533-040533 (2022)
9. J. Langdon, Z. Cui, A. Manthiram, ACS Energy Lett. **6**, 3809-3816 (2021)
10. G. Zhang, Y. Zhu, S. Lv, Z. Wang, P. Gao, *J.* Alloys Compd. **953**, 170134-170134 (2023)
11. S.H. Park, S.H. Kang, C.S. Johnson, K. Amine, M.M. Thackeray, Electrochem. Commun. **9**, 262-268 (2007)
12. P. Vanaphuti, Y. Liu, X. Ma, J. Fu, Y. Lin, J.Y Wen, Z. Yang, Y. Wang, *ACS Appl. Mater. Interfaces,* **13**, 22597-22607 (2021)
13. H. Pan, S. Jiao, Z. Xue, J. Zhang, X. Xu, L. Gan, Q. Li, Y. Liu, X. Yu, H. Li, L. Chen, Adv. Energy Mater. 13, 2203989-2203989 (2023)
14. D. Hlungwani, R.S. Ledwaba, P.E. Ngoepe, Mater. **15**, 5678-5678 (2022)
15. X. Li, Y. Xu, C. Wang, J. Alloys Compd. **479**, 310-313 (2009)
16. X. Hou, X. Liu, H. Wang, Z. Zhang, J. Zhou, M. Wang, *Energy Stor. Mater.* **57**, 577-606 (2023)
17. L. Xiong, Y. Xu, C. Zhang, Z. Zhang, J. Li, J Solid State Electr. **15**, 1263-1269 (2011)
18. E. Iwata, K.I. Takahashi, K. Maeda, T. Mouri, J. Power Sources. **81**, 430-433 (1999)
19. R.J. Gummow, A. De Kock, M.M. Thackeray, Solid State Ionics. **69**, pp. 59-67 (1994)
20. E. TobyáKelsey, N.H. áde Leeuw, J. Chem. Soc., Faraday Trans. **92**, 433-438 (1996)
21. A. Kuwabara, C.A. Fisher, Y.H. Ikuhara, H. Moriwake, H. Oki, Y. Ikuhara, RSC Adv. **2**, 12940-12948 (2012)
22. R.R. Maphanga, D.C. Sayle, T.X. Sayle, P.E. Ngoepe, Phys. Chem. Chem. Phys. **13**, 1307-1313 (2011)
23. T.X. Sayle, C.R.A. Catlow, R.R. Maphanga, P.E. Ngoepe, D.C. Sayle, J. Am. Chem. Soc. **127**, 12828-12837 (2005)
24. D. Hlungwani, R.S. Ledwaba, P.E. Ngoepe, PhD. Thesis. **1**, 1, (2023)
25. D.C. Sayle, R.L. Johnston, Curr. Opin. Solid State Mater. Sci. **7**, 3-12 (2003)
26. M.G.S.R. Thomas, W.I.F. David, J.B. Goodenough, P. Groves, Mater. Res. Bull. **20**, 1137-1146 (1985)
27. T.F. Yi, C.L. Hao, C.B. Yue, R.S. Zhu, J. Shu, Synth. Met. **159**, 1255-1260 (2009)
28. X.M. Wu, X.H. Li, Z.B. Xiao, J. Liu, W.B. Yan. M.Y. Ma, Mater. Chem. Phys. **84**, 182-186 (2004)
29. D. Mohanty, H. Gabrisch, Solid State Ion. **194**, 41-45 (2011)
30. S. Choi, A. Manthiram, J. Electrochem. Energy Convers. Storage. **27**, 215-224 (2006)
31. J. Shu, T.F. Yi, M. Shui, Y. Wang, R.S. Zhu, X.F. Chu, F. Huang, D. Xu., L. Hou, Comput. Mater. Sci. **50**, 776-779 (2010)